

Quaternary MgSiN₂-GaN alloy semiconductors for deep UV applications

Ozan Dernek* and Walter R. L. Lambrecht†

*Department of Physics, Case Western Reserve University,
10900 Euclid Avenue, Cleveland, OH-44106-7079*

Ultra-wide direct band gap semiconductors hold great promise for deep ultraviolet opto-electronic applications. Here we evaluate the potential of MgSiN₂-GaN alloys for this purpose. Although MgSiN₂ itself has an indirect gap ~ 0.4 eV below its direct gap of ~ 6.5 eV, its different sign lattice mismatch from GaN in two different basal plane directions could avoid the tensile strain which limits Al_xGa_{1-x}N on GaN for high x . Two octet-rule preserving structures (with space groups $Pmn2_1$ and $P1n1$) of a 50 % alloy of MgSiN₂ and GaN are investigated and are both found to have gaps larger than 4.75 eV using quasiparticle self-consistent (QS) *GW* calculations. Both are nearly direct gap in the sense that the indirect gap is less than 0.1 eV lower than the direct gap. Their mixing energies are positive yet small, with values of 8 (31) meV/atom for $Pmn2_1$ ($P1n1$) indicating only a small driving force toward phase separation.

I. INTRODUCTION

Compact light sources in the deep UV, in particular the UV-B and UV-C with wavelengths shorter than 315 nm and 280 nm respectively would have a large impact in science and technology [1]. Light emitting diodes (LED) in this range could fulfill this demand but require new semiconductor materials with efficient doping and band gaps $E_g > 4$ eV. The current prevailing approach toward this goal is to develop Al_xGa_{1-x}N alloys, which form a continuous alloy system with wurtzite structure and end point band gaps of 3.6 eV (GaN) and 6.3 eV (AlN). [2–6] However, high Al-content alloys suffer from a number of challenges: (1) epitaxial growth on GaN substrates results in tensile strain, which tends to develop cracks, (2) n-type doping with Si leads to distorted DX center with a deep level and hence inefficient doping, (3) p-type doping is even more problematic and (4) the inverted crystal field splitting of AlN leads to predominantly transverse magnetic (TM) light emission from the basal plane surface.[7, 8] Here we propose alloys of MgSiN₂ and GaN as an alternative to overcome at least some of these problems.

Heterovalent ternary semiconductors of the type II-IV-N₂ using group II and group-IV element pairs as a replacement for the group III element in III-N nitrides, have gained significant interest in recent years.[9–11] These materials have a wurtzite derived structure, which ideally consists in a fully ordered orthorhombic superlattice of wurtzite with space group #33 ($Pbn1$ in the setting with $a_o \approx 2a_w, b_o \approx \sqrt{3}a_w, c_o = c_w$ where a_w, c_w are the wurtzite and a_o, b_o, c_o the orthorhombic lattice constants, or $Pna2_1$ if a_o and b_o are reversed). They add significant flexibility to the chemical materials design space because one has a choice of II=Be, Mg, Zn, Cd and IV=Si, Ge, Sn. Furthermore, a certain degree of

polytypic disorder with space group #26 ($Pmc2_1$) which also satisfies the octet-rule [12], or the presence of exchange defects II_{IV} and IV_{II} can be tolerated and allows for some disorder tuning of the gap [13–16].

The design flexibility is further enhanced by considering mixed II-IV-N₂ with III-N alloy systems. Recently, the ZnGeN₂-GaN alloy system was investigated both computationally[17] and experimentally in thin film growth[18, 19]. In particular, it was found that at 50% two octet-rule preserving structures exist with space groups $Pmn2_1$ and $P1n1$, of which the former was found to have the lowest total energy. In the $Pmn2_1$ structure, each N is surrounded by exactly two Ga, one Zn and one Ge and the structure can be viewed as half a layer of ZnGeN₂ and half a layer of GaN in the b direction or a $[010]_{1/2}$ lattice.

Here we use this flexibility to search for a semiconductor which is closely lattice matched to GaN and has a gap exceeding 4 eV. From the band gap vs. equivalent wurtzite lattice constant diagram in Ref. 10, one can see that MgSiN₂ is significantly closer lattice matched to GaN than AlN and has a predicted direct gap of ~ 6.3 - 6.5 eV [20, 21]. Unfortunately, its indirect gap is about 0.4 eV lower, so it is actually an indirect gap semiconductor which is undesirable for light emission devices. Upon closer inspection of the lattice match, one should note that the equivalent wurtzite lattice constant in [10] was taken as $a_o/2$. However, inspecting the individual orthorhombic lattice constants, there is only a 1.1% mismatch of MgSiN₂ with respect to $2a_{\text{GaN}}$ in the a -direction, but a -4.7% mismatch in the b direction and a -4% mismatch in the c -direction. Nonetheless, these can be viewed as acceptable lattice mismatch compared with AlN which has a $-2.4, -3.9\%$ mismatch in a and c directions compared to GaN. In particular, a compressive strain in the basal plane would be less disadvantageous than a tensile strain and at least in one basal plane direction, the strain of MgSiN₂ on GaN would be compressive.

The indirect gap in MgSiN₂ results from the valence band maximum (VBM) occurring at $U = (\pi/a, 0, \pi/c)$ in the $Pbn2_1$ setting of the space group, while the con-

* ozan.dernek@case.edu

† walter.lambrecht@case.edu

TABLE I: Cohesive energies of each species calculated by QUESTAAL and QE. Species Ga, Mg, and Si are calculated in their bulk phases, and N₂ molecule calculated in a large vacuum cell. Spin-polarization is included for single atom calculations.

| Species | Space Group | Coh. En. (eV/atom) | | |
|---------|--------------------------------|--------------------|-------|-------|
| | | QUESTAAL | QE | Expt. |
| Ga | <i>Cmce</i> | -2.69 | -2.71 | -2.81 |
| Mg | <i>P6₃/mmc</i> | -1.50 | -1.50 | -1.51 |
| Si | <i>Fd$\bar{3}m$</i> | -4.56 | -4.62 | -4.63 |
| N | N ₂ | -5.04 | -5.18 | -4.92 |

duction band minimum (CBM) occurs at $\Gamma = (0, 0, 0)$. Considering the gap of GaN at U when calculated in an equivalent *Pbn*2₁ supercell, which lies 1.1 eV below the actual VBM at Γ , and interpolating the direct $\Gamma - \Gamma$ and indirect $U - \Gamma$ gaps linearly between MgSiN₂ and GaN, using a direct (indirect) gap of 3.4 (4.5) eV in GaN and 6.5 (6.1) in MgSiN₂ [20], one might expect a direct gap up to about 75% and a direct gap of 5.8 eV at that point. Of course, alloy band gaps typically show band gap bowing and the above also ignores strain effects. Nonetheless, this seemed sufficiently promising to investigate the band gap in a quaternary MgSiN₂-GaN system further.

II. COMPUTATIONAL METHOD

The stability of the 50% alloy is investigated by calculating first the cohesive energy vs. the isolated atoms, second, the energy of formation with respect to the elements in their standard state, and finally, the mixing energy vs. the two end compounds GaN and MgSiN₂. The total energies required for each system are calculated using density functional theory (DFT) within the Generalized Gradient Approximation (GGA) in the Perdew-Burke-Ernzerhof (PBE)[22] parametrization. The structural parameters, internal position and lattice constants were fully relaxed using the QUANTUM EXPRESSO code [23] within the Projector Augmented Wave (PAW) method. Subsequently they were also calculated using the all-electron QUESTAAL code which implements the full-potential linearized muffin-tin orbital (FP-LMTO) method. In evaluating the total energy differences between different systems, we took care of using exactly the same muffin-tin radii for the atoms in different systems and use exactly equivalent \mathbf{k} -point meshes and real space meshes to maximize systematic error cancellation. All, three systems, GaN, MgSiN₂ and MgSiGa₂N₄ were calculated in the same 16 atom cell to achieve equal convergence. The energy of formation calculations are done using the single atom energies calculated in large vacuum cells (with spin polarization for Ga, Si and N) and the most stable form of each species. The bulk formation energies are obtained using both code suites and compared to experimental values in Table I.

The band structures were calculated using the quasi-particle self-consistent (QS) *GW* approach [24, 25] implemented in the QUESTAAL code[26]. Here *GW* stands for the one-electron Green's function and *W* for the screened Coulomb interaction in Hedin's approach [27], which define the self-energy $\Sigma = iGW$. The difference between this non-local and energy dependent self-energy operator $\Sigma(\omega)$ and the exchange-correlation potential v_{xc} is, as usual, calculated within first-order perturbation theory starting from the DFT Kohn-Sham (KS) eigenvalues ϵ_i and eigenstates ψ_i . However, in the QS approach, a new energy independent but non-local potential, expressed by its matrix elements in the basis of KS eigenstates, $\tilde{\Sigma}_{ij} = \frac{1}{2}\text{Re}[\Sigma_{ij}(\epsilon_i) + \Sigma_{ij}(\epsilon_j)]$ is evaluated and iterated to convergence. Here $\text{Re}[\dots]$ means taking the hermitian part. The eigenvalues thereby become independent of the DFT starting point exchange-correlation choice. They are found to be typically somewhat overestimating band gaps because within standard *GW* the screening of the Coulomb potential is calculated in the random phase approximation (RPA) which underestimates screening. This can be overcome by adding ladder diagrams[28–30] but, as an alternative, it is found that using 80% of the $\tilde{\Sigma}$ and 20% DFT exchange correlation potential usually gives very accurate results for a wide variety of systems[31, 32]. We follow this approach here.

The QUESTAAL implementation of the *GW* approach uses a mixed interstitial plane wave, product basis set to expand two point quantities, such as $W = (1 - vP)^{-1}v$, with v the bare Coulomb interaction and $P = -iGG$, the polarization propagator. This is a more efficient basis set than plane waves to represent the screening and, as a result, high-energy states of the KS equation are less crucial to the convergence of the method. The use of an atom-centered basis set allows one to express the self-energy $\tilde{\Sigma}$ in real space and hence to interpolate for \mathbf{k} -points different from the ones for which $\Sigma(\mathbf{k}, \omega)$ is calculated. This way, accurate band dispersions along the symmetry lines and effective masses can be obtained. We tested convergence of the various parameters entering the *GW* calculations, finding a $3 \times 3 \times 3$ \mathbf{k} -mesh, *spdf - spd* basis set including Ga-*3d* local orbitals, and E_{max} above which the self-energy is approximated by an average value to be well converged. Details of the QSGW implementation can be found in Ref.[25].

III. RESULTS

We here present results for both the *Pmn*2₁ and *P1n1* structures, which were both found to have low energy in the ZnGeGa₂N₄ compound at 50% mixing. We start with the structural parameters, given in Table II. We compare the lattice constants with the Vegard's average. *Pmn*2₁ perfectly matches these values. When all the lattice constants and angles between them are relaxed, the *P1n1* structure slightly shifts into a monoclinic phase, with the angles between the lattice vectors $\alpha = \gamma = 90^\circ$

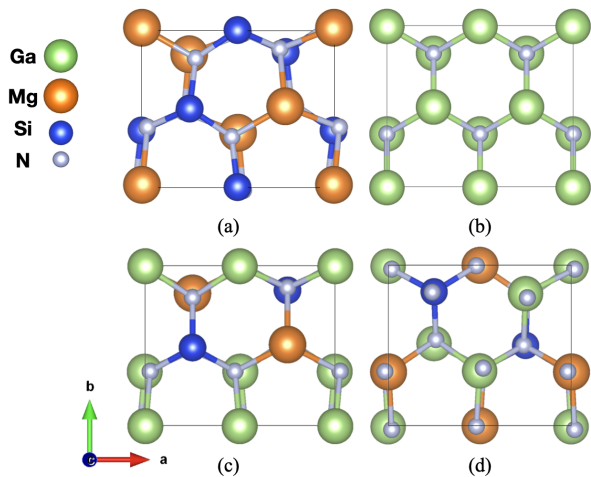


Fig. 1: Octet-rule-preserving $\text{MgSiGa}_2\text{N}_4$ structures in (c) $Pmn2_1$ and (d) $P1n1$ space groups and their relation to the compounds (a) MgSiN_2 and (b) GaN both in the $Pbn2_1$ structure.

and $\beta = 90.16^\circ$. This is consistent with the space group which belongs in the monoclinic crystal system. However, the change in the volume and total energy is negligible. Therefore we continue to investigate the material in its orthorhombic phase. The $P1n1$ lattice constant a falls out of the range set by GaN and MgSiN_2 , while b and c are very close to the GaN lattice constants. Yet the volume of the two structures are identical. The reduced coordinates for the atoms in the $Pmn2_1$ and for the $P1n1$ are provided in Table III and IV, respectively. Compared to experimental values, we may notice that the volume is overestimated by 2.1% for MgSiN_2 and by 2.8% for GaN . Thus, we also expect an overestimate by a similar amount for the 50% compound.

Next, we discuss the total energy results which allow us to ascertain the stability of the proposed alloy. Table V lists the cohesive energies, formation energies and mixing energies evaluated using both methods. Values obtained by the QE method are given in parenthesis. The formation energies give the energy difference with respect to the elements in their standard state at room temperature and atmospheric pressure. Their negative value indicate stability. A more strict criterion is to evaluate the mixing energy of the alloy with respect to the two separate compounds. These values are positive but quite small. This indicates, as usual for semiconductor alloys, that phase segregation is thermodynamically more stable. However, the values are quite small and indicate that there is only a weak driving force toward segregation.

Subsequently, we calculated their electronic band structures both in GGA and in the quasiparticle self-consistent GW approximations. The results of the band gaps are included in Table VI. The band gaps here do not include zero-point motion electron-phonon coupling corrections. In Ref. 20 these were estimated to be of

order -0.2 eV. On the other hand, the overestimate of the volume by about 2% leads to an underestimate of the band gap. Using the band gap deformation potential $dE_g/d\ln V$ of -8.7 eV [20], the volume correction would increase the gap by about 0.2 eV. Thus these two corrections nearly cancel each other. For GaN , likewise, our gap here is underestimated by about 0.2-0.3 eV because of our use here of the GGA volume. The band structures are shown in Fig 2. The overview band structure shows that the top set of valence bands between -8 and 0 eV are predominantly $\text{N-}2p$ like as expected for a nitride. These show projections on the local partial waves. Near the bottom of the valence band we can see that the states are bonding between $\text{N-}2p$ and $\text{Si-}s$ and $\text{Ga-}s$. The $\text{Mg-}s$ contribution is less strongly present. The conduction band minimum atomic orbital character is more readily seen in the colored bands which indicate the contribution of the $\text{Ga-}s$ muffin-tin-orbital basis functions. The corresponding $\text{Si-}s$ and $\text{Mg-}s$ are not shown but are significantly smaller. The predominant $\text{Ga-}s$ rather than Mg or $\text{Si-}s$ character of the CBM is consistent with a quantum well model. The $Pmn2_1$ is essentially an ultrathin superlattice of half unit cell GaN quantum wells and half unit cell MgSiN_2 units stacked along the \mathbf{b} -direction. The band offset is type I with a conduction band offset of about 1.4 eV according to Ref. [33]. Therefore, if the quantum well just captures a single bound state, it could be at about 1.4 eV above the GaN CBM. The quantum confined effects for the holes are expected to be smaller since the effective masses are much larger. The wider the barrier of MgSiN_2 in this case, the stronger the quantum confinement effects would be, hence the larger the gap of the $(\text{MgSiN}_2)_x(\text{GaN})_{1-x}$ alloys.

A zoom in near the VBM and CBM for both structures shows that the VBM does not occur at Γ but rather at Y and thus, strictly speaking, we still have an indirect gap system. However, this location of the VBM is different from that of MgSiN_2 , where it occurs at U and the energy difference between the VBM at Γ and Y here is very small. Furthermore, this is expected to be rather sensitive to strain. It also shows details of the crystal field splitting at Γ in $Pmn2_1$ structure. The PDOS in the CBM shows that near the CBM the $\text{N-}s$ partial waves dominate over the cation- s states but we should recall that these are anti-bonding s states and that the dominant $\text{Ga-}s$ muffin-tin-orbital (as shown from the band color) extends into the N spheres, thus also contribute to the $\text{N-}s$ PDOS.

The bands at Γ were symmetry labeled for $Pmn2_1$. The point group is C_{2v} . In this point group, Γ_1 (or a_1) correspond to the z basis function with x, y, z along (a, b, c) respectively, Γ_2 corresponds to b_2 or y and Γ_4 to b_1 or x . The a_2 or Γ_3 corresponds to xy basis function. The CBM has Γ_1 symmetry and is s -like. Thus allowed dipole transitions occur between the VBM at Γ and the the CBM for $\mathbf{E} \parallel \mathbf{c}$. For $\mathbf{E} \parallel \mathbf{b}$, the transitions occur from the VBM-1, and for $\mathbf{E} \parallel \mathbf{a}$ from the VBM-2. The valence band splittings are given in Table VII. We may also note

TABLE II: Average bond lengths and relaxed lattice constants in Å for compounds and MgSiGa₂N₄ structures. Unit cell volumes are compared with the Vegard's average of MgSiN₂ and GaN.

| | Mg-N (Å) | Ga-N | Si-N (Å) | <i>a</i> (Å) | <i>b</i> (Å) | <i>c</i> (Å) | Volume (Å ³) |
|---------------------------|----------|------|----------|--------------|--------------|--------------|--------------------------|
| MgSiN ₂ | 2.11 | | 1.76 | 6.504 | 5.310 | 5.031 | 173.75 |
| Expt | | | | 6.473 | 5.272 | 4.986 | 170.15 |
| GaN | | 1.96 | | 6.433 | 5.571 | 5.240 | 187.79 |
| Expt | | | 6.378 | 5.523 | 5.185 | 182.65 | |
| <i>Pmn</i> 2 ₁ | 2.06 | 1.95 | 1.75 | 6.467 | 5.440 | 5.147 | 181.07 |
| <i>P1n</i> 1 | 2.04 | 1.95 | 1.75 | 6.324 | 5.550 | 5.159 | 181.07 |
| Vegard's | | | | 6.469 | 5.441 | 5.136 | 180.75 |

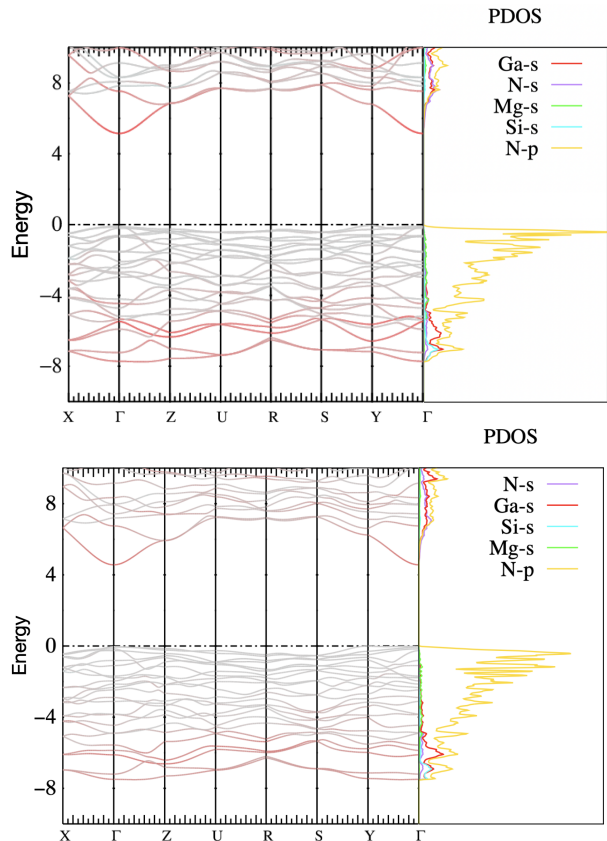


Fig. 2: Band structures and corresponding partial density of states are shown for both *Pmn*2₁ (top) and *P1n*1 (bottom) space group of MgSiGa₂N₄ alloys. The band structures are calculated in the 0.8Σ approximation, and Ga-*s* orbitals are color coded with red-scale while the rest of the orbitals are in gray-scale.

In both structures, the VBM is found to be on the *k*-point *Y*, but the difference between the VBM and highest valence band energy at Γ is less than 0.1 eV (Table VI). Partial density of states (in arbitrary but consistent units of states/cell per eV) are given for the orbitals of interest. The valence bands are dominated by the N-*p* orbitals (color gold), while the CBM consists of mostly Ga-*s* orbitals (color red).

TABLE III: Reduced coordinates of atoms for the *Pmn*2₁ structure.

| Atom | Wyckoff ^a | <i>x</i> | <i>y</i> | <i>z</i> |
|-----------------|----------------------|----------|----------|----------|
| Ga | 4b | 0.25162 | -0.32950 | 0.49925 |
| Mg | 2a | 0.00000 | 0.16007 | 0.49196 |
| Si | 2a | 0.00000 | -0.17887 | 0.00043 |
| N _{Ga} | 4b | 0.22286 | -0.32754 | 0.88188 |
| N _{Mg} | 2a | 0.00000 | 0.13495 | 0.90272 |
| N _{Si} | 2a | 0.00000 | -0.19564 | 0.34264 |

^a 2a positions are (*x,y,z*) and (1/2, -*y,z*+1/2), 4b positions are (*x,y,z*), (-*x*+1/2, -*y,z*+1/2), (*x*+1/2, -*y,z*+1/2), and (-*x,y,z*).

TABLE IV: Reduced coordinates of atoms for the *P1n*1 structure.

| Atom | Wyckoff ^a | <i>x</i> | <i>y</i> | <i>z</i> |
|------------------|----------------------|----------|----------|----------|
| Ga ₁ | 2a | 0.49984 | -0.15530 | -0.00064 |
| Ga ₂ | 2a | 0.74905 | -0.32606 | 0.49904 |
| Mg | 2a | 0.25124 | -0.33223 | 0.49367 |
| Si | 2a | 0.00024 | -0.16716 | 0.00067 |
| N _{Ga1} | 2a | 0.50965 | -0.13049 | 0.38153 |
| N _{Ga2} | 2a | 0.26846 | 0.30852 | 0.38142 |
| N _{Mg} | 2a | 0.73140 | 0.32936 | 0.40271 |
| N _{Si} | 2a | -0.00986 | -0.16526 | 0.34159 |

^a All atoms in 2a positions: (*x,y,z*), (-*x*+1/2, -*y,z*+1/2)

that the *z*-like Γ_1 state has the smallest mass along the $\Gamma - Z$ direction, while the next Γ_2 or *y*-like state has the smallest mass in the $\Gamma - Y$ direction and the Γ_4 or *x*-like state has its lowest mass in the $\Gamma - X$ direction. Unfortunately, the top of the VBM is thus *z*-like which implies that the same problem occurs as for Al_{*x*}Ga_{1-*x*}N at high Al-concentration *x*. Namely, the lowest energy transition is predominantly transverse magnetic (TM) which hinders light extraction for normal exit angle from the basal plane. However, this is sensitive to strain and the splitting between the Γ_2 and Γ_1 state is quite small and could perhaps more easily be reversed by some strain engineering.

For the *P1n*1-structure, we have only a double-glide mirror plane *n* perpendicular to the *b*-axis, so the point

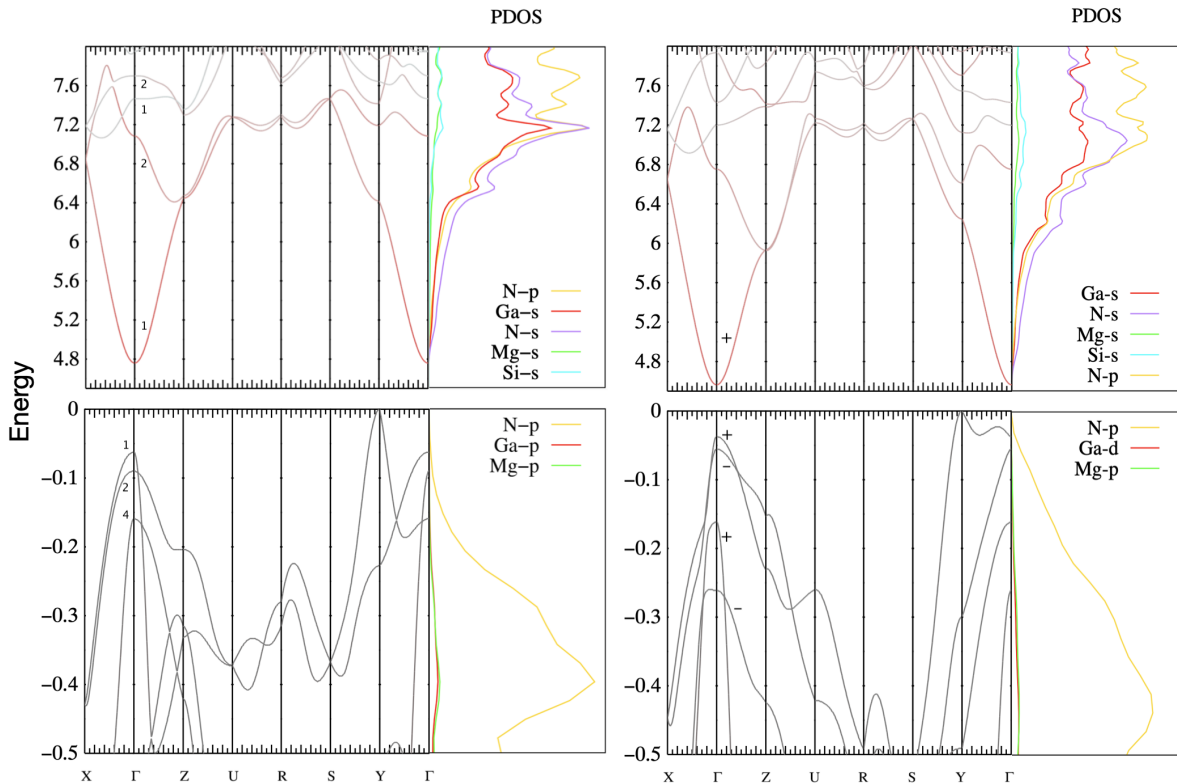


Fig. 3: Band splitting and their symmetries are shown for $Pmn2_1$ (left) and $P1n1$ (right) structures, along with the partial density of states of dominant orbitals. The same color coding as in Fig. 2 is used.

TABLE V: Cohesive energies, energy of formation, and mixing energies in GGA with units eV/atom. The values given in parenthesis obtained by the QE method.

| | MgSiN ₂ | GaN | $Pmn2_1$ | $P1n1$ |
|-----------|--------------------|---------------|---------------|---------------|
| E_{coh} | 5.25 (5.31) | 4.39 (4.42) | 4.82 (4.86) | 4.80 (4.84) |
| E_{for} | -1.19 (-1.19) | -0.94 (-0.47) | -0.90 (-0.83) | -0.88 (-0.81) |
| E_{mix} | | | 0.008 (0.007) | 0.029 (0.031) |

group is C_s and states can only be labeled as even or odd with respect to the n_y mirror-plane. Obviously, y orbitals are odd with respect to this mirror-plane while x and z are even. We can see some interesting changes in the band structure reflecting the lower symmetry. First, at Γ , there are now four states instead of three within the first 0.3 eV below the VBM. Along the $\Gamma - X$ line we can see that the top two bands cross, indicating that they have different irreducible representations, respectively $+$ and $-$. The next band down has $+$ symmetry and therefore an avoided crossing with the $+$ band emanating from the VBM at Γ . Along $\Gamma - Y$ however, there is no symmetry left at all and hence the top bands can repel each other while in the $Pmn2_1$ these bands were allowed to cross because of their different even or odd character with respect to the m_x mirror plane.

TABLE VI: Band gaps of compounds and alloys in various approximations.

| Compound | | GGA | 0.8Σ | $0.8\Sigma + \Delta(0)^a$ |
|---|----------|------|-------------|---------------------------|
| MgSiN ₂ | Indirect | 4.03 | 6.15 | 5.84 |
| MgSiN ₂ | Direct | 4.36 | 6.52 | 6.28 |
| GaN | Direct | 1.72 | 3.08 | |
| MgSiGa ₂ N ₄ ($Pmn2_1$) | Direct | 2.98 | 4.83 | |
| MgSiGa ₂ N ₄ ($Pmn2_1$) | Indirect | 2.92 | 4.76 | |
| MgSiGa ₂ N ₄ ($P1n1$) | Direct | 2.73 | 4.60 | |
| MgSiGa ₂ N ₄ ($P1n1$) | Indirect | 2.70 | 4.57 | |

^a $\Delta(0)$ is an estimated zero-point motion correction from Ref. [20]

We have also determined the effective mass tensors at the band edges, as given in Table VIII. The curvatures are determined by fitting the bands to a parabolic dispersion very close to the band edge in question in several directions and subsequently determining the principal values and direction of the constant energy surfaces. The conduction band mass tensor shows only slight anisotropy consistent with the point group symmetry. In the $P1n1$ case, one principal axis is along y , the other two can be at some angle from x in the xz plane because the point group is only C_s . For the CBM, we find these angles to be near 45° . The three highest valence bands at Γ show a larger anisotropy with the smallest negative

TABLE VII: Valence-band splittings (in meV) at the Γ point relative to actual VBM at Y .

| Symmetry | $Pmn2_1$ | Symmetry | $P1n1$ |
|------------|----------|----------|--------|
| Γ_1 | -63 | + | -37 |
| Γ_2 | -90 | - | -56 |
| Γ_4 | -159 | + | -162 |
| | | - | -261 |

mass occurring in the direction that corresponds to the irreducible representation of the band in question. In terms of the well known $\mathbf{k} \cdot \mathbf{p}$ expression for the inverse effective mass tensor,

$$M_{\alpha\beta}^{-1} = \delta_{\alpha\beta} \frac{1}{m_e} + \frac{1}{m_e^2} \sum_{n' \neq n} \frac{\langle n\mathbf{k}|p_\alpha|n'\mathbf{k}\rangle \langle n'\mathbf{k}|p_\beta|n\mathbf{k}\rangle + c.c.}{E_{n\mathbf{k}} - E_{n'\mathbf{k}}} \quad (1)$$

we can see that the interaction of the top valence band with the conduction band would give a small negative contribution to the M_{zz}^{-1} and none at all for M_{xx}^{-1} or M_{yy}^{-1} because only p_z matrix elements can couple the VBM of Γ_1 symmetry to the Γ_1 CBM. On the other hand, in the x (y) directions, there are valence band states just below it of symmetry Γ_4 (Γ_2) which will couple to the VBM of Γ_1 symmetry and hence give a large positive change in M_{xx}^{-1} or M_{yy}^{-1} . This means a large negative change in the mass itself because $\Delta(1/m) = -\Delta m/m^2$. Thus we find strongly negative masses for the x and y directions for the Γ_1 VBM. This implies a high positive hole mass in these directions. Other lower lying Γ_1 states will also give a negative contribution to the effective mass in the z direction but, because these states are farther away, they will result in a smaller negative mass in the z direction. Similar reasoning explains the other cases. For the Γ_2 second valence band, the Γ_1 state above it, which is the smallest energy difference, will give a strong negative contribution to M_{yy}^{-1} in the $\Gamma - Y$ direction so a positive change to the mass itself which must compensate the effect from bands of Γ_1 symmetry lying deeper in the valence band. Hence the smallest mass along the y direction for the state of Γ_2 or y symmetry. For the $P1n1$ case, the top valence band along y is seen to have a positive curvature because of the strong repulsion of the two valence bands along this symmetry line. For the mass tensor at Y we can see for $Pmn2_1$ that $(m_x m_y m_z)^{1/3} = 1.09$, so the effective average density of states mass is close the free electron mass. For the $P1n1$ structure the effective density of states mass is 1.48, thus somewhat higher. While the conduction band masses are similar, they are also nearly isotropic.

Finally, we make an estimate of the band gap bowing in the alloy system. The band gap is estimated as $E_g(x) = E_g(0) + xE_g(1) - bx(1-x)$. For the direct $\Gamma - \Gamma$ gap we find $x \approx 0.6$ eV, while for the $U - \Gamma$ gap it is about 0.7 eV. The results are shown in Fig. 4. They show that a band crossing between direct and indirect gap still occurs at about $x = 0.75$ with a gap as high as 5.6 eV at this

TABLE VIII: Electron effective masses (in units of free electron mass m_e) at Γ for CBM, and top valence bands in close vicinity to VBM are given for $Pmn2_1$ and $P1n1$ structures. The mass tensor components at the true VBM at Y are also given. The negative values for valence bands indicate positive hole masses. For the orthorhombic case ($Pmn2_1$), the principal axes are along the crystal axes x, y, z corresponding to a, b, c ; for the $P1n1$ monoclinic space group, one principal axis is along y , the others in the xz plane make an angle α_x from the x axis as indicated.

| | CBM | Γ_1 | Γ_4 | Γ_2 | Y | |
|------------|-------|------------|------------|------------|--------|--------|
| m_x | 0.244 | -3.059 | -3.887 | -0.272 | -0.714 | |
| m_y | 0.257 | -11.302 | -0.224 | -4.321 | -1.105 | |
| m_z | 0.226 | -0.196 | -2.567 | -2.494 | -1.666 | |
| | CBM | +1 | -1 | +2 | -2 | Y |
| m_1 | 0.243 | -0.286 | -0.459 | -0.196 | -2.372 | -0.664 |
| α_x | -43.6 | 2.5 | -3.7 | 91.2 | -87.8 | 0.5 |
| m_2 | 0.240 | -2.988 | -3.936 | -2.652 | -2.652 | -1.627 |
| α_x | 46.4 | 92.5 | 86.3 | 1.2 | 2.2 | 89.5 |
| m_y | 0.264 | 2.167 | -0.948 | -2.348 | -0.251 | -3.025 |

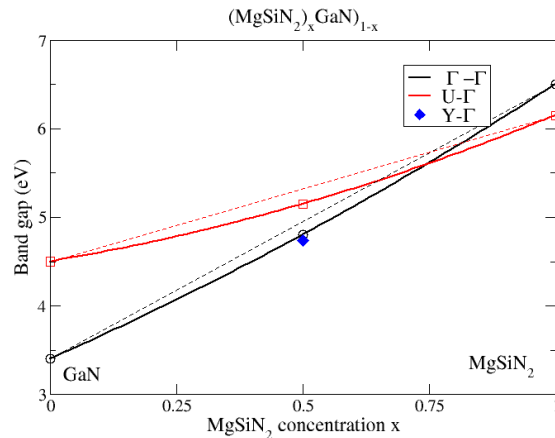


Fig. 4: Band gaps in the $(MgSiN_2)_x(GaN)_{1-x}$ alloy system.

point. We note that in principle, octet-rule conserving superlattice type structures with half unit cells of $MgSiN_2$ and GaN stacked along the b direction as building blocks can be designed.[17]

IV. CONCLUSIONS

We have shown that a 50% alloy of $MgSiN_2$ and GaN is promising as an alternative to $Al_xGa_{1-x}N$ alloy for increasing the gap beyond that of GaN to allow for optoelectronic applications into the deep UV region. First, we find that two octet-ruling compounds exist with the

composition $\text{MgSiGa}_2\text{N}_4$ which have negative energies of formation and only a small positive mixing energy with respect to GaN and MgSiN_2 . In its lowest energy structure with space group $Pmn2_1$, the lattice constant in the a direction has only a +0.5 % mismatch with the corresponding lattice constant in GaN and the positive sign indicates that on a GaN substrate this compound would be under compression in this direction. In the other direction in the basal plane, its mismatch is -2.3% . The band gap of this structure is nearly direct, by which we mean that the indirect gap is less than 0.1 eV below the direct gap at Γ , and the direct gap is calculated to be 4.83 eV. Another structure with space group $P1n1$ also has fairly good lattice mismatch from GaN and a nearly direct gap of 4.76 eV. These small deviations from direct gap character could possibly be overcome by strain tuning.

We should point out some caveats here. For a quaternary system, achieving the precise $Pmn2_1$ ordering is

even more challenging than for a ternary and going away from the perfect 50% stoichiometry of MgSiN_2 - $(\text{GaN})_2$ would likely introduce even more cation disorder. This is expected to decrease the band gap somewhat but gaps larger than 4 eV are still expected. To facilitate comparison with future experimental realization of these materials we have provided ample detail on their predicted crystal structure and band structure, including the effective mass tensors at the band edges.

ACKNOWLEDGMENTS

The calculations were performed on the High Performance Computing Resource in the Core Facility of Advanced Research Computing at Case Western Reserve University. This work was supported by the US Department of Energy Basic Energy Sciences (DOE-BES) under grant number DE-SC0008933.

-
- [1] M. Kneissl, T.-Y. Seong, J. Han, and H. Amano, The emergence and prospects of deep-ultraviolet light-emitting diode technologies, *Nature Photonics* **13**, 233 (2019).
- [2] M. Crawford, Chapter One - Materials Challenges of AlGa_N-Based UV Optoelectronic Devices, in *III-Nitride Semiconductor Optoelectronics*, Semiconductors and Semimetals, Vol. 96, edited by Z. Mi and C. Jagadish (Elsevier, 2017) pp. 3–44.
- [3] T. Detchprohm, X. Li, S.-C. Shen, P. Yoder, and R. Dupuis, Chapter Four - III-N Wide Bandgap Deep-Ultraviolet Lasers and Photodetectors, in *III-Nitride Semiconductor Optoelectronics*, Semiconductors and Semimetals, Vol. 96, edited by Z. Mi and C. Jagadish (Elsevier, 2017) pp. 121–166.
- [4] M. Shatalov, R. Jain, T. Saxena, A. Dobrinsky, and M. Shur, Chapter Two - Development of Deep UV LEDs and Current Problems in Material and Device Technology, in *III-Nitride Semiconductor Optoelectronics*, Semiconductors and Semimetals, Vol. 96, edited by Z. Mi and C. Jagadish (Elsevier, 2017) pp. 45–83.
- [5] H. Hirayama, Chapter Three - Growth of High-Quality AlN on Sapphire and Development of AlGa_N-Based Deep-Ultraviolet Light-Emitting Diodes, in *III-Nitride Semiconductor Optoelectronics*, Semiconductors and Semimetals, Vol. 96, edited by Z. Mi and C. Jagadish (Elsevier, 2017) pp. 85–120.
- [6] S. Zhao and Z. Mi, Chapter Five - Al(Ga)N Nanowire Deep Ultraviolet Optoelectronics, in *III-Nitride Semiconductor Optoelectronics*, Semiconductors and Semimetals, Vol. 96, edited by Z. Mi and C. Jagadish (Elsevier, 2017) pp. 167–199.
- [7] J. Zhang, H. Zhao, and N. Tansu, Effect of crystal-field split-off hole and heavy-hole bands crossover on gain characteristics of high Al-content AlGa_N quantum well lasers, *Applied Physics Letters* **97**, 111105 (2010).
- [8] C. Reich, M. Guttman, M. Feneberg, T. Wernicke, F. Mehnke, C. Kuhn, J. Rass, M. Lapeyrade, S. Einfeldt, A. Knauer, V. Kueller, M. Weyers, R. Goldhahn, and M. Kneissl, Strongly transverse-electric-polarized emission from deep ultraviolet AlGa_N quantum well light emitting diodes, *Applied Physics Letters* **107**, 142101 (2015).
- [9] W. R. L. Lambrecht and A. Punya, Heterovalent ternary II-IV-N₂ compounds: perspectives for a new class of wide-band-gap nitrides, in *III-Nitride Semiconductors and their Modern Devices*, edited by B. Gill (Oxford University Press, 2013) Chap. 15, pp. 519–585.
- [10] S. Lyu, D. Skachkov, K. Kash, E. W. Blanton, and W. R. L. Lambrecht, Band gaps, band-offsets, disorder, stability region, and point defects in II-IV-n₂ semiconductors, *Physica Status Solidi (a)* **216**, 1800875 (2019).
- [11] A. D. Martinez, A. N. Fioretti, E. S. Toberer, and A. C. Tamboli, Synthesis, structure, and optoelectronic properties of II-IV-V₂ materials, *J. Mater. Chem. A* **5**, 11418 (2017).
- [12] P. C. Quayle, E. W. Blanton, A. Punya, G. T. Junno, K. He, L. Han, H. Zhao, J. Shan, W. R. L. Lambrecht, and K. Kash, Charge-neutral disorder and polytypes in heterovalent wurtzite-based ternary semiconductors: The importance of the octet rule, *Phys. Rev. B* **91**, 205207 (2015).
- [13] D. Skachkov, P. C. Quayle, K. Kash, and W. R. L. Lambrecht, Disorder effects on the band structure of ZnGe_2 : Role of exchange defects, *Phys. Rev. B* **94**, 205201 (2016).
- [14] S. Lany, A. N. Fioretti, P. P. Zawadzki, L. T. Schelhas, E. S. Toberer, A. Zakutayev, and A. C. Tamboli, Monte Carlo simulations of disorder in ZnSnN_2 and the effects on the electronic structure, *Phys. Rev. Materials* **1**, 035401 (2017).
- [15] J. J. Cordell, G. J. Tucker, A. Tamboli, and S. Lany, Bandgap analysis and carrier localization in cation-disordered ZnGeN_2 , *APL Materials* **10**, 011112 (2022).
- [16] T. D. Veal, N. Feldberg, N. F. Quackenbush, W. M. Linhart, D. O. Scanlon, L. F. J. Piper, and S. M. Durbin, Band Gap Dependence on Cation Disorder in ZnSnN_2 Solar Absorber, *Advanced Energy Materials* **5**, 1501462 (2015).
- [17] B. H. D. Jayatunga, S. Lyu, S. K. Radha, K. Kash, and

- W. R. L. Lambrecht, Ordering in the mixed ZnGeN₂-GaN alloy system: Crystal structures and band structures of ZnGeGa₂N₄ from first principles, *Phys. Rev. Materials* **2**, 114602 (2018).
- [18] B. H. D. Jayatunga, M. R. Karim, R. A. Lalk, O. Ohanaka, W. R. L. Lambrecht, H. Zhao, and K. Kash, Metal-Organic Chemical Vapor Deposition of ZnGeGa₂N₄, *Crystal Growth & Design* **20**, 189 (2020).
- [19] T. Suehiro, M. Tansho, and T. Shimizu, Quaternary Wurtzitic Nitrides in the System ZnGeN₂-GaN: Powder Synthesis, Characterization, and Potentiality as a Photocatalyst, *The Journal of Physical Chemistry C* **121**, 27590 (2017).
- [20] A. P. Jaroenjittichai and W. R. L. Lambrecht, Electronic band structure of Mg-IV-n₂ compounds in the quasiparticle-self-consistent *gw* approximation, *Phys. Rev. B* **94**, 125201 (2016).
- [21] J. B. Quirk, M. Räsander, C. M. McGilvery, R. Palgrave, and M. A. Moram, Band gap and electronic structure of MgSiN₂, *Applied Physics Letters* **105**, 112108 (2014).
- [22] J. P. Perdew, K. Burke, and M. Ernzerhof, Generalized gradient approximation made simple, *Phys. Rev. Lett.* **77**, 3865 (1996).
- [23] P. Giannozzi, S. Baroni, N. Bonini, M. Calandra, R. Car, C. Cavazzoni, D. Ceresoli, G. L. Chiarotti, M. Cococcioni, I. Dabo, A. Dal Corso, S. de Gironcoli, S. Fabris, G. Fratesi, R. Gebauer, U. Gerstmann, C. Gougoussis, A. Kokalj, M. Lazzeri, L. Martin-Samos, N. Marzari, F. Mauri, R. Mazzarello, S. Paolini, A. Pasquarello, L. Paulatto, C. Sbraccia, S. Scandolo, G. Sclauzero, A. P. Seitsonen, A. Smogunov, P. Umari, and R. M. Wentzcovitch, Quantum espresso: a modular and open-source software project for quantum simulations of materials, *Journal of Physics: Condensed Matter* **21**, 395502 (19pp) (2009).
- [24] M. van Schilfgaarde, T. Kotani, and S. Faleev, Quasiparticle Self-Consistent *GW* Theory, *Phys. Rev. Lett.* **96**, 226402 (2006).
- [25] T. Kotani, M. van Schilfgaarde, and S. V. Faleev, Quasiparticle self-consistent *GW* method: A basis for the independent-particle approximation, *Phys. Rev. B* **76**, 165106 (2007).
- [26] D. Pashov, S. Acharya, W. R. Lambrecht, J. Jackson, K. D. Belashchenko, A. Chantis, F. Jamet, and M. van Schilfgaarde, Questaal: A package of electronic structure methods based on the linear muffin-tin orbital technique, *Computer Physics Communications*, 107065 (2019).
- [27] L. Hedin, New method for calculating the one-particle green's function with application to the electron-gas problem, *Phys. Rev.* **139**, A796 (1965).
- [28] B. Cunningham, M. Grüning, P. Azarhoosh, D. Pashov, and M. van Schilfgaarde, Effect of ladder diagrams on optical absorption spectra in a quasiparticle self-consistent *GW* framework, *Phys. Rev. Materials* **2**, 034603 (2018).
- [29] B. Cunningham, M. Gruening, D. Pashov, and M. van Schilfgaarde, QSGW: Quasiparticle Self consistent *GW* with ladder diagrams in W (2021), preprint arXiv 2106.05759.
- [30] S. K. Radha, W. R. L. Lambrecht, B. Cunningham, M. Grüning, D. Pashov, and M. van Schilfgaarde, Optical response and band structure of LiCoO₂ including electron-hole interaction effects, *Phys. Rev. B* **104**, 115120 (2021).
- [31] C. Bhandari, M. van Schilfgaarde, T. Kotani, and W. R. L. Lambrecht, All-electron quasiparticle self-consistent *GW* band structures for SrTiO₃ including lattice polarization corrections in different phases, *Phys. Rev. Materials* **2**, 013807 (2018).
- [32] D. Deguchi, K. Sato, H. Kino, and T. K. Ni, Accurate energy bands calculated by the hybrid quasiparticle self-consistent *GW* method implemented in the ecalj package, *Japanese Journal of Applied Physics* **55**, 051201 (2016).
- [33] S. Lyu and W. R. L. Lambrecht, Band alignment of III-N, ZnO and II-IV-N₂ semiconductors from the electron affinity rule, *Journal of Physics D: Applied Physics* **53**, 015111 (2019).